Modeling the performance of an ideal NaBH$_4$–H$_2$O$_2$ direct borohydride fuel cell

Richard O. Stroman [a, b, *], Gregory S. Jackson [a, 1]

[a] Department of Mechanical Engineering, University of Maryland, College Park, MD 20742, United States
[b] Chemistry Division, US Naval Research Laboratory, Washington, DC 20375, United States

HIGHLIGHTS

- A 2-D model of an ideal direct borohydride fuel cell has been developed.
- 2-D effects such as boundary layer development are explored.
- The model is used for cell-level design analysis.

ARTICLE INFO

ABSTRACT

A 2D direct borohydride fuel cell (DBFC) model has been developed to explore the prospective performance of this technology, for a cell with fast selective electrocatalysts and a selective membrane. In the modeled DBFC, a Nafion membrane in the Na$^+$ form separates flow channels with aqueous fuel (0.1–0.5 M NaBH$_4$/4 M NaOH) and oxidizer (4 M H$_2$O$_2$/4 M H$_2$SO$_4$). Electrochemical reactions occur on catalyst-coated channel walls. The electrocatalysts are selective for complete BH$_4^-$ oxidation and H$_2$O$_2$ reduction, the reactions have fast forward rate constants, and only Na$^+$ and H$_2$O cross the membrane. The model captures interfacial charge transfer reactions and complex transport in the flow channels and membrane. Results show that current density and voltage efficiency vary by >50% from inlet to outlet due to concentration boundary layer development. The BH$_4^-$ concentration boundary layer limits peak power density, despite migration and fuel utilizations below 10%. Power density increases with BH$_4^-$ inlet concentration and fuel flow rate, but at the expense of lower fuel utilization. Water crosses the membrane up to 14 times its production rate at the anode. Low fuel utilization and water imbalance suggest the importance of system designs with reactant recirculation and water recovery.
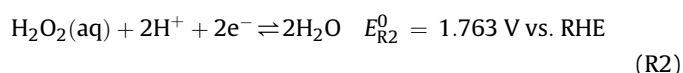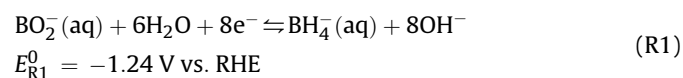
Published by Elsevier B.V.

1. Introduction

The direct borohydride fuel cell (DBFC) configuration in this study, illustrated in Fig. 1, uses a Nafion membrane in the Na$^+$ form to separate flow channels containing aqueous fuel (0.1–0.5 M NaBH$_4$/4 M NaOH) and oxidizer (4 M H$_2$O$_2$/4 M H$_2$SO$_4$) solutions. Borohydride (BH$_4^-$) is oxidized on the anode catalyst at the fuel channel wall and hydrogen peroxide (H$_2$O$_2$) is reduced on the cathode catalyst at the oxidizer channel wall. The catalyst-coated channel walls function as current collectors. DBFC experiments

using alkaline NaBH$_4$ and acidic H$_2$O$_2$ solutions with Nafion membranes [1–3] and similar separated electrode cell topologies [1,4–6] have been reported in the literature.

In an ideal DBFC, complete BH$_4^-$ oxidation (Reaction (R1)) yields 8e$^-$ with a standard reduction potential of E^0_{R1}, and complete H$_2$O$_2$ reduction in acidic media (Reaction (R2)) yields 2e$^-$ with a standard reduction potential of E^0_{R2} [7].

$$BO_2^-(aq) + 6H_2O + 8e^- \leftrightarrows BH_4^-(aq) + 8OH^-$$
$$E^0_{R1} = -1.24 \text{ V vs. RHE} \tag{R1}$$

$$H_2O_2(aq) + 2H^+ + 2e^- \rightleftharpoons 2H_2O \quad E^0_{R2} = 1.763 \text{ V vs. RHE} \tag{R2}$$

The electrochemical circuit is closed by sodium (Na$^+$) crossing the membrane, which also drives a net water flux from fuel solution to oxidizer solution via electro-osmotic drag. The net reaction

* Corresponding author. Chemistry Division, US Naval Research Laboratory, Washington, DC 20375, United States. Tel.: +1 (202) 767 3115; fax: +1 (202) 404 8119.
E-mail address: richard.stroman@nrl.navy.mil (R.O. Stroman).
[1] Present address: Mechanical Engineering Department, Colorado School of Mines, Golden, CO, United States.
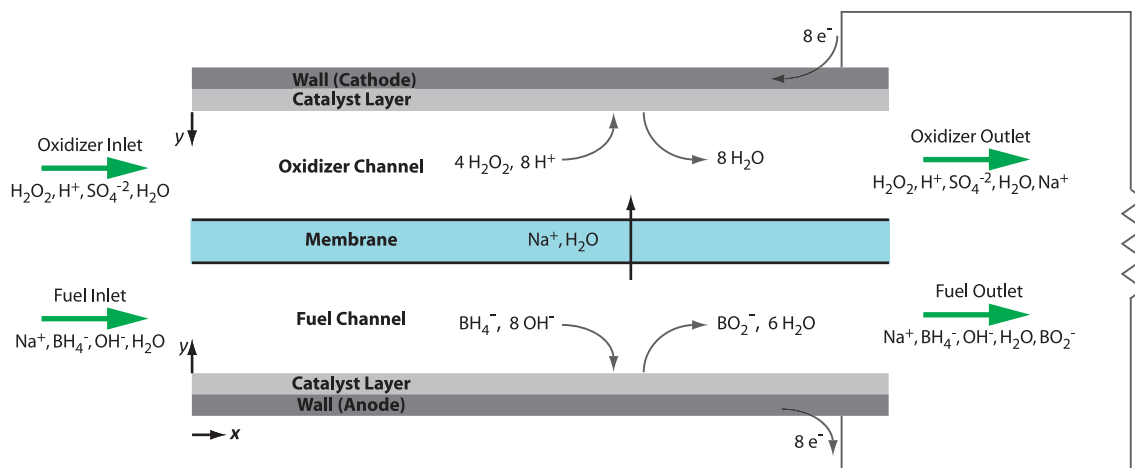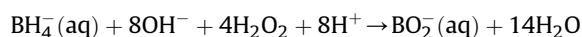
Fig. 1. Cell geometry, model domain and electrochemical reactions.

(Reaction (R3)) consumes BH_4^- and OH^- at the anode and H_2O_2 and H^+ at the cathode to produce BO_2^- and H_2O, with a theoretical cell potential of E^0_{R3}.

$$BH_4^-(aq) + 8OH^- + 4H_2O_2 + 8H^+ \rightarrow BO_2^-(aq) + 14H_2O$$
$$E^0_{R3} = 3.01 \text{ V}$$

(R3)

This DBFC differs from common low temperature fuel cells such as the proton exchange membrane fuel cell (PEMFC) and direct methanol fuel cell (DMFC). The catalyst in PEMFCs and DMFCs is on the membrane to enable H^+ participation in the electrochemical reactions, but the catalyst in this DBFC can be elsewhere because the aqueous electrolytes in each channel support ion transport. Channel transport in PEMFCs and DMFCs is governed by convection and diffusion, but in a DBFC migration also contributes. Finally, slower diffusion in the liquid phase favors development of steeper concentration gradients in a DBFC.

Interest in DBFCs has grown due to several desirable features of this technology. The reactants can be stored at sufficiently high concentrations to give theoretical energy densities greater than state-of-the-art rechargeable batteries [8]. The aqueous reactant solutions can be stored at ambient temperature and pressure. The theoretical cell voltage is 3.01 V when the oxidizer is H_2O_2 in acidic media, which substantially exceeds cell voltages of H_2–O_2 fuel cells. In addition, the reactant chemical energy can be converted directly to electricity without any chemical preprocessing, thereby reducing power system complexity and improving reliability. Despite these advantages, challenges remain before DBFCs can realize their theoretical promise. Continued progress toward meeting those challenges has promoted interest in DBFCs for applications where energy density is important, particularly for air-independent propulsion, remote sensors and portable electronics.

For DBFC systems to be practical, higher performance electrocatalysts and membranes must be developed [9,10]. Experiments reported in the literature show poor catalytic activity and the loss of reactants to unproductive side reactions. BH_4^- crossover has been reported, leading to mixed potentials and decreased cell voltage. Membrane conductivity suffers due to the low mobility of large ions (such as Na^+) in common membrane materials.

Reactions (R1) through (R3) assume complete oxidation of BH_4^- at the anode and reduction of H_2O_2 at the cathode. In practice, there are intermediate steps and competing reactions which can occur at each electrode. At the anode, the complex network of charge-transfer steps and other non-electrochemical catalytic reactions that constitute the borohydride oxidation mechanism are still a matter of debate. Reaction (R1) describes the ideal global oxidation reaction, but the $8e^-$ are likely provided to the anode through a series of single electron transfers involving intermediate species adsorbed on the electrocatalyst surface and in solution [11,12]. The intermediate species provide opportunities for alternative reaction pathways, some involving chemical steps which do not yield electrons to the anode. An analogous situation exists at the cathode, for which Reaction (R2) describes the ideal global H_2O_2 reduction reaction.

Despite a lack of consensus in the literature as to the detailed borohydride oxidation mechanism, a system of three competing reactions has been used to describe the processes occurring at a DBFC anode. The first reaction is (R1). The second reaction is borohydride hydrolysis (Reaction (R4)), in which the anode catalyst accelerates the chemical conversion of BH_4^- to BO_2^-. Hydrolysis is undesirable because it uselessly consumes fuel and can produce bubbles which inhibit the transport of BH_4^- to the electrocatalyst surface for Reaction (R1).

$$BH_4^-(aq) + 2H_2O \rightarrow BO_2^-(aq) + 4H_2$$

(R4)
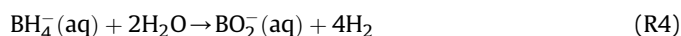
The third reaction is hydrogen oxidation (Reaction (R5)), which can consume H_2 produced by Reaction (R4) and recover electrons that would otherwise be lost.

$$2H_2O + 2e^- \rightleftharpoons H_2 + 2OH^-(aq) \quad E^0_{R5} = -0.828 \text{ V vs. RHE}$$

(R5)
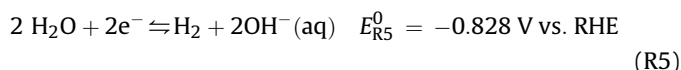
The net result of Reactions (R1), (R4) and (R5) depends on the anode potential and species concentrations in solution. Reaction (R1) dominates when the BH_4^- concentration is low, the hydroxide concentration is high, or the electrode potential is substantially less negative than E^0_{R1} [13]. When these conditions are not met, adsorbed hydrogen can accumulate on the anode electrocatalyst, shifting the net reaction in favor of Reaction (R4) as adsorbed hydrogen forms H_2 rather than water [14]. Reaction (R5) contributes electrons to the anode at potentials less negative than E^0_{R5} and consumes electrons at more negative potentials.

The undesirable hydrolysis reaction effectively reduces the number of electrons n_{elec} produced per BH_4^- fuel molecule consumed. Ideally, the cell is operated such that Reaction (R1) goes to completion and $n_{elec} = 8$, but many operating conditions lead to intermediates that favor Reaction (R4) and thereby reduce n_{elec} and

the power generated by the DBFC. The power is reduced not only by the lower current but also by the mixed potentials that arise due to the intermediate species and multiple oxidation reactions. Several boron-containing intermediate species have been proposed. One example is BH_3OH^-, whose oxidation may be rate limiting to Reaction (R1) at low anode potentials [15] and whose hydrolysis may be a key contributor to the extent of Reaction (R4) [16].

The BH_4^- oxidation pathways are controlled in part by the selection of anode catalyst, with Au and Pt having received the most attention [17]. Recent studies have focused on alloys and nano-structured catalysts with improved activity and/or selectivity for BH_4^- electrochemical oxidation [17–19]. The various metallic electrocatalysts differ in their activity for Reactions (R4) and (R5) with Ag and Au being the least active and Pt- and Pd-based electrocatalysts being the most active for both reactions [15,18,20]. The relative rates for the global Reactions (R1) and (R4) with a given catalyst depend on the anode potential, BH_4^- concentration and solution pH with increased pH improving selectivity for Reaction (R1) [8]. The anode reaction can be approximated by the ideal electrochemical oxidation (R1) for many conditions. For example, Au anodes, in spite of their lower activity, are highly selective for Reaction (R1) when the BH_4^- concentration is low relative to the OH^- concentration [13]. However, the same study showed that BH_4^- concentrations above 20% of the OH^- concentration lead to significant H_2 evolution because Au does not oxidize H_2 well. On more active Pt- and Pd-based electrocatalysts, the range of operating conditions that facilitate the complete Reaction (R1) are limited because these catalysts have higher activity than Au for the hydrolysis reaction. However, if the cell is operated at high current densities where the anode potential is less negative than E^0_{R5}, active catalysts such as Pt and some of its alloys readily drive the reverse of Reaction (R5) [15,21]. Thus, at higher current densities the full BH_4^- oxidation with n_{elec} approaching eight can be achieved [22] if the catalyst layer is designed to ensure good access of OH^- to the catalyst. High current densities favor full oxidation in part by maintaining low concentrations of BH_4^- near the anode due to transport limitations in the presence of excess OH^-.

The combination of charge-transfer and chemical catalytic reactions at the cathode can be described by three reactions analogous to Reactions (R1), (R4) and (R5) at the anode. The first cathode reaction is the complete reduction of H_2O_2 in an acidic medium in Reaction (R2). The second reaction, (R6), is the heterogeneous chemical decomposition of H_2O_2 into O_2 and water, accelerated by the cathode electrocatalyst. Reaction (R6) at the cathode is analogous to Reaction (R4) at the anode.

$$2\ H_2O_2\ (aq) \rightarrow O_2 + 2H_2O \qquad (R6)$$

Like Reaction (R4), the H_2O_2 decomposition Reaction (R6) reduces the number of electrons per reactant molecule consumed. Similarly, Reaction (R6) can produce gaseous O_2, which can occlude the cathode catalyst. Cathode design can mitigate this problem, and at adequately low cathode potentials, O_2 produced by Reaction (R6) may be reduced electrochemically at the cathode by Reaction (R7) to recover the otherwise lost electrons.

$$O_2 + 2H^+ + 2e^- \leftrightharpoons 2\ H_2O_2(aq) \quad E^0_{R7} = 0.695\ V\ vs.\ RHE \quad (R7)$$
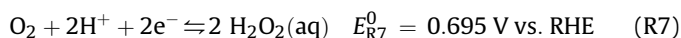
Experiments with DBFC chemistries different from this study have been reported in the literature. The fuel solution in a DBFC consists of aqueous BH_4^- and OH^- ions with an alkali metal cation, and while Li^+ and K^+ have been suggested, the most common is Na^+ [9,23]. DBFC fuel solutions include OH^- as a reactant and stabilizer for BH_4^-, which can be stored for months in high pH media (pH $\geq$13) [24,25]. A range of oxidizers has explored, including O_2 (in air or pure) and H_2O_2 [9,10]. When H_2O_2 is chosen, it can be stored

in acidic or alkaline media. Acidic solutions provide higher standard half-cell potential for H_2O_2 reduction (1.763 V vs. RHE) than alkaline solutions (0.870 V vs. RHE) [7]. Alkaline solutions offer ways to mitigate system-level problems such as volume imbalance due to water crossover through the membrane [6]. Among acidic media, some anions impede Reaction (R2) more than others, with the best activity occurring in the hydrohalic acids HI, HBr, and HCl [26,27]. However, a common choice among experiments reported in the literature is H_2SO_4.

Alternative cell geometries and topologies have also been explored. Experimental results have been published for cells with a catalyst layer on the channel wall [1,6], catalyst coated on the membrane [23,28,29] and catalyst distributed throughout the channel on a porous medium [4,30]. The relative strengths and weaknesses of the different electrocatalyst locations for both the anode and the cathode are not clear because of the lack of good models or direct experimental comparison.

While there has been significant work on the electrochemistry of DBFCs, practical DBFC cell design and operating spaces have not been explored as thoroughly. Experiments on fundamental kinetics as well as electrode geometry have provided some insight into what is feasible for DBFCs, but relationships between cell designs and performance are not understood. The complex coupling of the reaction pathways with transport through reactant concentrations, particularly for the anode, raise many questions as to how to translate the numerous electrocatalyst kinetic studies into predicting cell performance for practical design. The range of reactant and product concentrations along the flow path of a practical cell with substantial reactant utilization can have a significant impact on reaction overpotentials and transport limitations, and thus overall cell efficiencies and power densities. Understanding such relationships is critical for practical DBFCs to achieve their promising potential. In this regard, carefully constructed numerical models of DBFCs can explore cell configurations and designs that provide preferred conditions for coupling complex transport with the kinetics to favor the highest power densities and the most effective conversion of fuel and oxidizer to useful energy (i.e., efficiency). A model can also provide state information that is useful for understanding how the cell operates, but is otherwise difficult to measure. This study presents a 2-D steady state finite volume model to explore how cell geometry and operating conditions impact DBFC performance under conditions which favor Reactions (R1) and (R2). The specific goals of this work were:

1. Explore the performance that may become available if efforts to improve DBFC electrocatalysts and membranes are successful.
2. Understand trends relating DBFC cell design parameters to performance, so that cells can be designed to favor conditions in which Reactions (R1) and (R2) predominate.

The modeled system is ideal in that only Reactions (R1) and (R2) take place, and the membrane is permeable only to Na^+ and water. Realistically, improved electrocatalysts and membranes are unlikely to eliminate Reactions (R4)–(R7) and the transport of species other than Na^+ through the membrane. The results presented here represent the performance of an ideal DBFC, which realistic DBFC performance may approach as the technology improves.

DBFC models have been published prior to this work. Verma and Basu [31] modeled an O_2 DBFC consisting of a Nafion membrane in contact with porous catalyst layers and a well-mixed volume of fuel. Mass transport to the cathode was governed by Fick's law (O_2 diffusion in air) and transport to the anode was neglected. All charge transport processes in the cell were described by a fit to measurements of ohmic resistance. Sanli et al. [32] published a similar model, but with H_2O_2 as the oxidizer and mass transport

neglected entirely. Both [31] and [32] ignore down-the-channel effects. Shah et al. [33] published the most detailed DBFC model to date, for a cell topology similar to that of PEMFCs. The cell consisted of a Nafion membrane with a porous catalyst layer on each side; the catalyst layers were separated from reactant flow channels by porous diffusion layers. The model predicts cell voltage at a given current density by calculating activation and ohmic overpotentials explicitly as functions of current density, and then subtracting the overpotentials from the open circuit voltage. Concentration overpotentials were included by estimating concentrations near the electrodes, and using those concentrations in the calculation of activation overpotentials. Species concentrations were assumed to be uniform in the flow channels, but transport from the flow channels to the catalyst layer was approximated by a Nernst diffusion layer thickness correlation. Down-the-channel effects were not addressed. Of prior DBFC models, only one [34] included transport in a meaningful way and none addressed down-the-channel effects on cell performance. No prior DBFC model has studied the geometry depicted in Fig. 1.

Other fuel cell topologies and chemistries have been studied using 2-D finite volume models. A relevant example is that of Sprague and Dutta [35,36], who modeled a fuel cell similar to Fig. 1 with the exception that it had no membrane. The cell had a single liquid electrolyte and electrically neutral fuel and oxidizer species which reacted in a generalized way governed by the Frumkin–Butler–Volmer equation. The Poisson–Nernst–Plank equations were solved to resolve electrochemical double layers near the electrodes and the distributions of species and charge in the channel. The model presented here is solved in a similar way, but it differs from that of Sprague and Dutta in several key aspects. The model in this study includes a membrane, has different electrolytes and chemistries (specific to a DBFC) at the anode and cathode, and solves for the electric field by explicitly enforcing electroneutrality rather than by solving Poisson's electrostatic equation.

This work goes beyond previous DBFC modeling studies by examining a new cell topology, including down-the-channel effects with a 2-D model, and exploring the impacts of cell geometry and operating parameters on performance. The model here provides a framework in which to study cell performance under conditions where complete borohydride oxidation and complete hydrogen peroxide reduction are good approximations for the electrode reactions. The model can provide DBFC developers with guidance on how the complex coupling of transport and chemistry impacts practical cell design. This study establishes a basis for further studies incorporating more realistic chemistry and alternative cell configurations that can accelerate practical DBFC development.

2. Mathematical model

The steady state performance of a DBFC is modeled with a 2-D finite volume approach. The model domain includes two rectangular channels separated by a membrane and channel walls which function as electrodes (see Fig. 1). An aqueous fuel solution containing Na^+, OH^-, BH_4^-, and BO_2^- enters the anode channel and an aqueous oxidizer solution containing H_2O_2, H^+, and SO_4^{2-} enters the cathode channel. Both solutions flow in the same direction. Charge transfer reactions take place at the channel walls while Na^+ passes through a Nafion membrane in the Na^+ form from fuel channel to oxidizer channel.

The operating conditions and cell geometry in this study enable several simplifications. The fuel and oxidizer solutions are liquids and therefore effectively incompressible. The flows in the reactant channels are laminar because the Reynolds numbers are less than 150. The fuel and oxidizer solutions are electrically neutral because the electrochemical double layers are thin and treated as part of the

electrode interfaces. The electrodes are good electrical conductors and therefore all points along the channel for each electrode share the same electric potential. Homogeneous reactions may take place in the fuel and oxidizer solutions, but at high pH (pH >13) in the fuel and low pH (pH <1) in the oxidizer they occur so slowly in comparison to the electrode reactions that they can be neglected without significantly impacting the results [24,25]. The membrane is fully hydrated Nafion 115 (145 μm thick) in the Na^+ form, which is thin enough to make x-direction fluxes in the membrane insignificant.

Four simplifying assumptions accommodate unknown transport parameters:

- All activity coefficients are 1, i.e. the fuel and oxidizer solutions are ideal electrolytes.
- Only Na^+ and H_2O pass through the membrane (negligible BH_4^- crossover).
- Solution viscosity is the same as pure water.
- Heat is removed quickly enough to maintain isothermal conditions.

2.1. Model geometry, state variables and solution approach

The model domain is subdivided into channels and interfaces. Channels are discretized into numerical cells with state variables for pressure, x- and y-direction mass-averaged velocities, electric potential, and species mass fraction. Nomenclature for the state variables and other model parameters is provided in Appendix A. Fig. 1 shows orientations of the x- and y-coordinates. Velocity storage locations are staggered from scalar variables by one-half discretization to avoid odd–even decoupling. All interfaces are broken into discrete line segments (numerical cells) having state variables for electric potential and species mass fractions. The membrane interface also stores pressure.

The numerical grid density varies linearly in the x- and y-directions with the highest density near the inlet, electrodes and membranes to capture the development of entrance effects and boundary layers. Trial and error showed that consistent results are achieved when the smallest x-discretization is 0.25 times the mean x-discretization length and the smallest y-discretization is 0.10 times the mean y-discretization length. The grid density was increased until the solution achieved grid independence. Results presented here require 49,800 state variables to simulate a 200 mm long channel broken into 150 x-discretizations and 17 y-discretizations.

A solution is the set of state variable values which conserve mass, momentum, species and charge and are consistent with the boundary conditions. From a top-level point of view, the total cell current is calculated for specified cell voltage, geometry and operating conditions. The model is set up in MATLAB and solved using a Newton solver in KINSOL. KINSOL is a non-linear equation solver available from the Lawrence Livermore National Laboratory as part of a collection of equation solving tools called SUNDIALS [37]. The MATLAB code sets up the model geometry, discretizes the domain, applies boundary conditions, and provides a function KINSOL calls to evaluate the residuals (errors) associated with each prospective solution. KINSOL runs until the residual 2-norm is driven below a specified threshold (typically 10^{-3}), at which point the solution has been found. Solution time using one 3.3 GHz Xeon processor core is typically ~80 min, but it is reduced to ~40 min when the initial guess is from a solution for similar conditions.

2.2. Governing equations and boundary conditions

The residual for each state variable is the error in the associated governing equation. The state variables require governing

equations: conservation of mass (associated with pressure), conservation of momentum (associated with velocity), conservation of species (associated with mass fraction) and electroneutrality (associated with electric potential). Boundary conditions are applied at the inlets, outlets, electrodes, electrode interfaces and membrane interfaces. Some variables have one simple boundary condition and others have multiple mixed boundary conditions which are linked across interfaces by the related fluxes.

2.2.1. Pressure

Pressure is associated with mass conservation because mass fluxes are predominantly driven by pressure gradients. At steady state, mass conservation in the channels is the sum of mass fluxes across the boundaries of a numerical cell, therefore the residuals associated with mass conservation are:

$$R_{ch}^{P} = -\nabla \cdot \vec{J} \tag{1}$$

Mass conservation is also used to solve for pressure at the membrane interfaces, where two fluxes in the y-direction are involved (one mass flux from the channel and one from the membrane):

$$R_{m\_int}^{P} = \vec{J}_{ch} - \vec{J}_{mem} \tag{2}$$

The x-direction pressure boundary condition is constant pressure at the outlets ($P = 100$ kPa). The y-direction pressure boundary conditions are zero pressure gradient at the electrode ($\partial P/\partial y = 0$) in recognition of the zero net mass flux there.

2.2.2. Mass fractions

Species concentrations are derived from species conservation, which is written in terms of mass fraction to simplify the mass and momentum conservation equations. The concentration of species k is calculated from mass fraction by $C_k = \rho Y_k / W_k$. The species conservation equation is the sum of species flux and storage terms: $0 = \nabla \cdot \vec{J}_k + \partial(\rho Y_k)/\partial t$. The storage term can be rearranged to isolate $\partial Y_k/\partial t$ on the left hand side, which should be zero at steady state and becomes the mass fraction residual. The mass storage term $R_{ch}^{P} = \partial \rho/\partial t$ is zero at steady state, but it is retained to improve solver convergence by maintaining the link between species and mass conservation. The mass fraction residual for species k in the channel is therefore:

$$R_{k,ch}^{MF} = \frac{1}{\rho}\left(-\nabla \cdot \vec{J}_k - Y_k R_{ch}^{P} \right) \tag{3}$$

Species conservation is also used to find mass fraction residuals at the electrode and membrane interfaces, but it becomes a flux match because the interfaces have only two species fluxes and no mass storage term. At the electrode interfaces there is one flux from the channel and one flux from the electrode (due to reactions there) for each species k:

$$R_{k,e\_i}^{MF} = \vec{J}_{k,ch} - \vec{J}_{k,rxn} \tag{4}$$

Mass fraction residuals at the membrane interfaces involve one flux from the channel and one through the membrane for each species k.

$$R_{k,m\_i}^{MF} = \vec{J}_{k,ch} - \vec{J}_{k,mem} \tag{5}$$

The x-direction mass fraction boundary conditions are specified at the inlet for each species k based on the fuel and oxidizer concentrations. The y-direction mass fraction boundary conditions are the mass fractions at the electrode and membrane interfaces

Table 1
Velocity boundary conditions. The x-coordinate runs from inlet to outlet and the y-coordinate runs from electrode to membrane, as in Fig. 1.

Boundary	Description	Boundary condition(s)
Channel inlets	Fully developed with specified volumetric flow rate	$v_x = 1.5\ \mathrm{V}\,(1 - (2y/h - 1)^2)$ $v_y = 0$
Channel outlets	Fully developed	$\partial v_x/\partial x = 0$, $\partial v_y/\partial x = 0$,
Electrode interface	No slip condition Impermeable boundary	$v_x = 0$ $v_y = 0$
Membrane interface	No slip condition No gradient in membrane	$v_x = 0$ $\partial v_y/\partial y = 0$

dictated by the respective flux matches. Ultimately, the mass fractions on each side of the membrane are related by the membrane species fluxes, and mass fractions at the electrodes are related to the electrode potential boundary conditions by the reaction rates.

2.2.3. Velocity

Momentum conservation in the channels can be written as the sum of advection, pressure, diffusion and electric body force terms:

$$\frac{\partial(\rho \vec{v})}{\partial t} = -\nabla \rho \vec{v} \cdot \vec{v} - \nabla P + \mu \nabla^2 \vec{v} - \rho_c \nabla \phi \tag{6}$$

The electric body force term $\rho_c \nabla \phi$ accounts for the influence of the electric potential gradient on ions in solution. Taking only components involved in the x-direction momentum balance and rearranging to obtain $\partial v_x/\partial t$ (which should be zero at steady state) yields the x-direction velocity residual in the channels:

$$R_{ch}^{xM} = \frac{1}{\rho}\left[-\frac{\partial}{\partial x}(\rho v_x|v_x|) - \frac{\partial}{\partial y}(\rho v_x v_y) - \frac{\partial P}{\partial x} + \mu\left(\frac{\partial^2 v_x}{\partial x^2} + \frac{\partial^2 v_x}{\partial y^2}\right) \right.$$
$$\left. - \rho_c\frac{\partial \phi}{\partial x} - v_x R_{ch}^{P} \right] \tag{7}$$

The mass conservation storage term R_{ch}^{P} is retained in equation (7) for the same reasons as in equation (3). The y-direction velocity residuals R_{ch}^{yM} have the same form as equation (7):

$$R_{ch}^{yM} = \frac{1}{\rho}\left[-\frac{\partial}{\partial x}(\rho v_y v_x) - \frac{\partial}{\partial y}(\rho v_y|v_y|) - \frac{\partial P}{\partial y} + \mu\left(\frac{\partial^2 v_y}{\partial x^2} + \frac{\partial^2 v_y}{\partial y^2}\right) \right.$$
$$\left. - \rho_c\frac{\partial \phi}{\partial y} - v_y R_{ch}^{P} \right] \tag{8}$$

Velocity and pressure gradients in the x-direction are estimated by upwind differencing because transport in the x-direction is dominated by advection, and upstream state variables have more influence over advection than downstream state variables [38]. Velocity and pressure gradients in the y-direction are estimated by center differencing because they are small and transport in the y-direction is dominated by diffusion and migration. Velocity boundary conditions were assigned at the channel inlets, outlets and interfaces as shown in Table 1.

2.2.4. Electric potential

The electric potential in an electrolyte solution is related to the net charge density by Poisson's electrostatic equation.

$$\nabla^2 \phi = -\frac{\rho_c}{\varepsilon\varepsilon_0} \tag{9}$$

The small permittivity of free space ($\varepsilon_0 = 8.85419 \times 10^{-12}\,\text{F m}^{-1}$) makes the electric field gradient sensitive to any deviation from electroneutrality, and in real systems such deviations only occur in electrochemical double layers. Elsewhere the net charge density can be assumed to be zero [39]. Some models [35] have solved equation (9) in order to resolve double layers, but in this work the double layers are considered part of the interfaces, so the electric potential is found by enforcing electroneutrality. The electric potential residual is equal to the net charge density (i.e. deviation from electroneutrality) and is given by equation (10), which is solved to find the electric potential in the channels and at the interfaces.

$$R^\phi = F \sum_k z_k C_k \tag{10}$$

Charge conservation implies that the total anode current must equal the total cathode current at steady state. The electroneutrality condition ensures the total electrode currents are equal by conserving charge throughout the model domain.

The x-direction boundary conditions on electric potential are zero electric field at the inlets and outlets ($\partial\phi/\partial x = 0$) and the y-direction boundary conditions are the electrode potentials. The anode electric potential is zero to establish a reference for the system, and the cathode electric potential is the specified cell voltage.

2.3. Species, mass and charge fluxes in the channels

The species, mass and charge fluxes crossing scalar numerical cell boundaries must be calculated in order to evaluate the related conservation equation residuals. Solute species mole fluxes in the channel are described by the Nernst–Plank equation (equation (11)) which includes contributions from diffusion, migration and advection.

$$\vec{J}_k = -D_k \nabla C_k - z_k u_k F C_k \nabla\phi + \rho Y_k \vec{v}/W_k \tag{11}$$

Since diffusion cannot produce a net mass flux, the water diffusion mass flux is made equal to the negative sum of solute diffusion mass fluxes. Water has no net charge, so the migration term is dropped from the total water mole flux in equation (12).

$$\vec{J}_{H_2O} = \frac{1}{W_{H_2O}} \left(\sum_{k \neq H_2O} (W_k D_k \nabla C_k) + \rho Y_{H_2O} \vec{v} \right) \tag{12}$$

The total mass flux is the molecular mass weighted sum of the mole fluxes:

$$\vec{J} = \sum_k W_k \vec{J}_k \tag{13}$$

Table 2
Diffusivities and apparent molar volumes of fuel and oxidizer solutes.

Species	Diffusivity in H_2O at infinite dilution and 298 K [$m^2\,s^{-1} \times 10^9$]	Apparent volume in H_2O at infinite dilution and 298 K [$m^3\,kmol^{-1} \times 10^3$]
BH_4^-	2.42 [46]	−5.83[a]
BO_2^-	0.814 [47]	−14.5 [48]
H^+	9.312 [39]	0 [48]
H_2O_2	1.19 [49]	22.17 [49]
Na^+	1.334 [39]	−1.11 [48]
OH^-	5.260 [39]	−4.18 [48]
SO_4^{2-}	0.625 [50]	24.8 [51]

[a] Value unavailable but estimated to be smaller than BO_2^- by the diffusivity ratio.

Table 3
Thermophysical and transport properties in fully hydrated Nafion 115 in the Na^+ form at 298 K.

Property	Value
Na^+ mobility, $u_{Na^+,mem}$	$2.7 \times 10^{-8}\,m^2\,V^{-1}\,s^{-1}$ [52]
H_2O permeability, ρ_{H_2O}	$1.7 \times 10^{-14}\,m\,Pa^{-1}\,s^{-1}$ [53]
Na^+ concentration, $C_{Na^+} = C_{SO_3^-}$	$1.13\,kmol\,m^{-3}$ [54]
Na^+–H_2O electro-osmotic drag coefficient in fully hydrated Nafion in the Na^+ form, n_d	$9.2\,kmol\,H_2O/kmol\,Na^+$ [52]

The total charge flux is a charge-weighted sum of the mole fluxes:

$$\vec{J}_c = F \sum_k z_k \vec{J}_k \tag{14}$$

Equations (9)–(14) require concentration and electric potential gradients at the discretization boundaries. Gradients are estimated by center differencing because it tends to be more numerically stable for diffusion and migration [38]. Table 2 lists the transport and thermophysical properties appearing in equations (11)–(14).

2.4. Species and charge fluxes through the membrane

A 1-D sub-model was used to calculate the Na^+ and H_2O mole fluxes across a fully hydrated Nafion 115 membrane at each point down the channel. BH_4^- crossover through Nafion membranes has been observed in experiments [5,40], but was omitted because BH_4^- migration fluxes are oriented from cathode to anode, so the rate of crossover should be small at operating conditions far from OCV [40] where the electric potential gradient in the membrane is large. Table 3 lists transport parameters in the membrane sub-model.

Diffusion and migration drive Na^+ through the membrane, so the net Na^+ mole flux from fuel channel to oxidizer channel is given by equation (15):

$$\vec{J}_{Na,mem} = -D_{Na}\frac{dC_{Na}}{dy} - z_{Na} u_{Na} F C_{Na}\frac{d\phi}{dy} \tag{15}$$

The concentration and electric potential gradients are found by assuming linear profiles in the y-direction between the membrane interfaces. To maintain electroneutrality, the concentration of Na^+ must be equal to the concentration of SO_3^- groups: $C_{Na^+} = C_{SO_3^-}$.

Water can cross the membrane due to diffusion, permeation and electro-osmotic drag induced by the Na^+ flux. Water diffusion is neglected because the concentrations on each side of the membrane are nearly the same. Thus, the net water flux is determined by the permeation and electro-osmotic drag terms.

$$\vec{J}_{H_2O,mem} = -p_{H_2O}\Delta P \frac{\rho_{H_2O}}{W_{H_2O}} + n_d \vec{J}_{Na,mem} \tag{16}$$

2.5. Species and charge fluxes at the electrodes

Multiple charge transfer reactions can take place at an electrode simultaneously; the rate of each reaction can be modeled as the sum of an anodic reaction rate supplying electrons to the electrode and a cathodic rate removing electrons. The rate r of reaction q is given by equation (17), in which subscripts a and c refer to anodic and cathodic rate parameters, respectively.

$$r_q = k_{q,a} \prod_k C_k^{g_{k,q,a}} e^{n_{e,q}\beta_{q,a} f \Delta\phi} - k_{q,c} \prod_k C_k^{g_{k,q,c}} e^{n_{e,q}\beta_{q,c} f \Delta\phi} \tag{17}$$

Both terms in the rate expression depend on a rate constant k, local species concentrations C_k, reaction rate orders with respect to each species g_k, number of electrons transferred in the rate limiting step n_e, charge transfer symmetry factor β and the electric potential difference between the electrode and electrolyte $\Delta\phi$.

The net flux of species k at the electrode is needed to solve the species conservation equation at the electrode interface (equation (4)). The net species flux is the sum of contributions from each reaction occurring at the electrode as shown in equation (18); each contribution depends on a reaction rate r_q, stoichiometry $\nu_{k,q}$ and roughness factor ℓ. The roughness factor accounts for the difference between electrochemical and geometric electrode surface area.

$$\vec{J}_{k,\text{rxn}} = \ell \sum_q r_q \nu_{k,q} \tag{18}$$

The net current density at the electrode is found by summing the current density contributions from each species:

$$i_{\text{net}} = F \sum_k \vec{J}_{k,\text{rxn}} z_k \tag{19}$$

An advantage of this approach is that it accommodates mixed potentials, which is not possible with the traditional Butler–Volmer approach because the equilibrium potential cannot be predicted by thermodynamics. The present work assumes only one reaction takes place at each electrode, but the model could be expanded to describe the influence of competing reactions and intermediates if the rate parameters were known.

A disadvantage of this approach is that it requires rate parameters (k and β), which are rarely known. Since the goal of this work is to identify performance trends, the reaction rate values are less important than capturing the correct functional dependencies. The following educated guesses were made for reaction rate parameters:

- $n_{e,q}$ is set to 1 because it is assumed the overall rate is determined by an intermediate step which transfers one electron.
- $\beta_{q,a}$ and $\beta_{q,c}$ are set to 0.5 – a common assumption in the absence of known values. [41].
- For the borohydride oxidation reaction (Reaction (R1)), the anodic rate is assumed to be first order with respect to $C_{\text{BH}_4^-}$ and C_{OH^-} and the cathodic rate is assumed to be first order with respect to $C_{\text{BO}_2^-}$. There is experimental evidence for the first order dependency on $C_{\text{BH}_4^-}$ [42].
- For the hydrogen peroxide reduction reaction (Reaction (R2)), the anodic rate is assumed to be first order with respect to C_{H^+} and $C_{\text{H}_2\text{O}_2}$ and the cathodic rate has no concentration dependence.

2.6. Composition equation of state

The fuel and oxidizer solutions are incompressible, but an equation of state is still needed to relate solution mass density to composition. A state equation (equation (20)) relates solution mass density to mass fraction by accounting for the apparent molar volume of each solute.

$$\rho = \frac{\rho_{\text{H}_2\text{O}}}{Y_{\text{H}_2\text{O}} + \rho_{\text{H}_2\text{O}} \sum_k (\delta_k Y_k / W_k)} \tag{20}$$

$\rho_{\text{H}_2\text{O}}$ varies with temperature via a polynomial fit to empirical data at 100 kPa.

3. Results and discussion

This study consists of a baseline case and 12 alternative cases in which one parameter is altered (see Table 4) to identify the effects it has on DBFC performance. Many parameters remained the same in all cases (see Table 5). The model was run repeatedly for each case, first with a cell voltage of 3.4 V and then decreasing the cell voltage in 0.1 V steps until it reached the transport limited current density. Each run yielded values for all state variables in the model domain and post processing provided the mass, momentum and charge fluxes (i.e. current density). The state variables and fluxes were used to estimate performance metrics such as voltage efficiency, power density and fuel utilization.

Baseline values for the channel dimensions, membrane thickness and inlet flow rates were based on typical values appearing in published experimental studies. The inlet BH_4^- concentrations were chosen to operate in a regime where complete borohydride oxidation (Reaction (R1)) is likely to dominate the anode reactions (at cell voltages other than open circuit). Fast forward reaction rate constants ($k_{1,a}$ at the anode and $k_{2,c}$ at the cathode) were chosen to model the performance of a cell with an advanced electrocatalyst and emphasize the influence of transport.

3.1. Baseline case

Voltage efficiency is the ratio of actual cell voltage to the ideal open circuit voltage (OCV) predicted by thermodynamics. The voltage losses in a DBFC stem primarily from the following: 1) competing electrochemical reactions that depress OCV by shifting the equilibrium potentials of the anode and cathode, 2) activation overpotentials to drive electrons across electrode-solution interfaces, 3) changes in concentration near the electrodes as concentration gradients develop to drive fluxes to or from the electrodes, and 4) ohmic overpotentials to drive charge from anode to cathode.

The voltage losses (as in all fuel cells) increase with cell current density, which can be visualized by a polarization curve; the calculated baseline polarization curve is shown in Fig. 2(a). The cell voltages in Fig. 2(a) are useful in a relative sense because the model neglects fuel crossover and competing electrochemical reactions, but the slopes of the polarization curve in the linear region at intermediate current densities and in the transport-limited region at the highest current densities are credible because they are largely dictated by known transport parameters. The product of cell voltage and average current density gives an average cell area power density (W m^{-2} of electrolyte membrane), which provides a

Table 4
Baseline case and variations from the baseline.

Parameter	Baseline	Variations from baseline
Anode inlet [NaBH$_4$]	0.3 M	0.1, 0.2, 0.4, 0.5 M
Channel depth	1 mm	0.50, 0.75 mm
Membrane thickness	145 μm	1.45, 72.50 μm
Inlet fuel flow rate	60 mL min^{-1}	15, 30 mL min^{-1}
Forward reaction rate constants	10^6 m^4 mol^{-1} s^{-1}	10^0, 10^3 m^4 mol^{-1} s^{-1}

Table 5
Parameters common to all cases.

Parameter	Value
Anode inlet [NaOH]	4.0 M
Anode inlet [NaBO$_2$]	10^{-6} M
Channel width	10 mm
Temperature	298 K
Cathode inlet [H$_2$SO$_4$]	4.0 M
Cathode inlet [H$_2$O$_2$]	4.0 M
Oxidizer inlet flow rate	60 mL min^{-1}
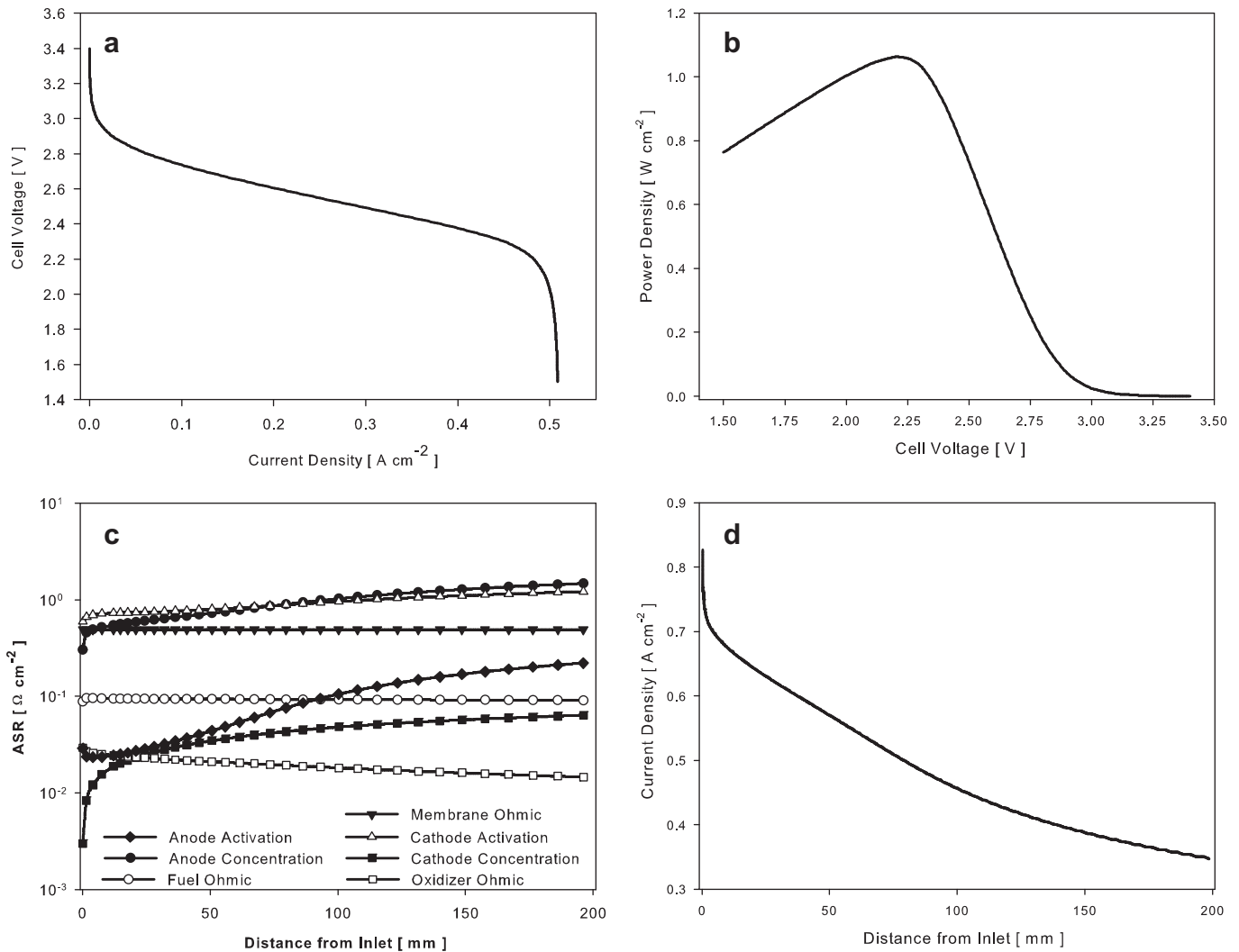
Fig. 2. (a) Baseline polarization curve showing activation, ohmic and concentration overpotentials. (b) Baseline power density vs. cell voltage. Points to the right of 2.2 V offer the best combination of power density and voltage efficiency. (c) Area specific resistance (ASR) associated with each overpotential at points down the channel, in the baseline case at 2.2 V. (d) Baseline current density at 2.2 V at points down the channel, which correlates with the rate of reactant consumption. Anode and cathode current densities at each point are the same to within 0.01%.

link to stack (volume) power density (W m^{-3}). Plotting cell area power density vs. cell voltage as in Fig. 2(b) illustrates the tradeoffs between power density and voltage efficiency. Fig. 2(b) shows baseline peak power density occurs at 2.2 V. Operating at cell voltages higher than 2.2 V offers the best combination of power density and efficiency.

The voltage losses due to activation, concentration and ohmic resistance vary along the channel with local concentrations and current density. The magnitude of each loss can be characterized by the associated area specific resistance (ASR). Fig. 2(c) plots the variation of the ASRs for each electrode and the membrane along the channel at a cell voltage of 2.2 V. For the baseline reaction rates, the ASRs for concentration in the fuel channel and cathode activation are largest, indicating they contribute most to losses in the fuel cell at this operating point. Both activation and concentration ASRs increase down the channel as concentration boundary layers lower the availability of reactants at the electrodes and depress the actual OCV further from the ideal OCV. Fig. 2(c) shows the importance of variation down the channel in a DBFC, which can only be captured with a multi-dimensional model.

The variation down the channel in the anode concentration ASR is explained in Fig. 2(d), which shows current density as a function of distance along the channel. BH$_4^-$ is consumed rapidly near the channel inlet but the consumption rate falls at points approaching the outlet. Thus, while channel fuel utilization (fuel consumed over fuel in) increases with lengthening the channels, the increased length results in lower power densities. The channel fuel utilization in the case shown in Fig. 2(d) is 4.4%. As seen in Fig. 2(c), the fuel channel concentration ASR becomes higher than other resistances with distance along the channel due to the growing thickness in the fuel concentration boundary layer. Transport through this boundary layer in the y-direction is complicated because advection, diffusion and migration all generate BH$_4^-$ fluxes in the y-direction. Fig. 3 shows anode channel BH$_4^-$ fluxes in the y-direction, mid-way between the inlet and outlet, at a cell voltage of 2.2 V. Transport at the anode surface is dominated by diffusion because the concentration of BH$_4^-$ there is nearly zero, but migration plays a significant role in the center of the channel where the concentration is higher and the electric field drives BH$_4^-$ toward the anode.

Transport of other species also impacts the DBFC performance. In particular, transport of Na$^+$ and H$_2$O through the membrane produces an advection flux that increases with current density. In the channel, this advection flux carries all species, including BH$_4^-$ as shown in Fig. 3. Since this model assumes only Na$^+$ and H$_2$O pass
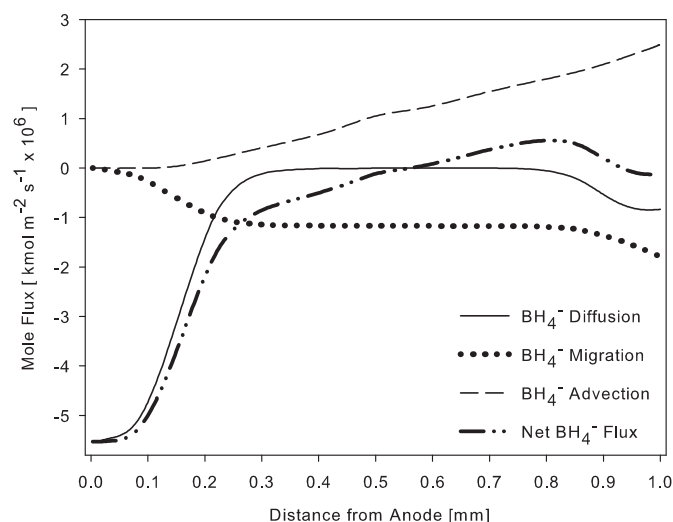
Fig. 3. Mole fluxes of BH_4^- in the y-direction, half way down the anode channel, as a profile from anode to membrane. Positive fluxes are toward the membrane and negative fluxes are toward the anode. Results for the baseline case at 2.2 V (peak power density).

through the membrane, the net flux of BH_4^- at the membrane interface must be zero, which can only be satisfied with an elevated BH_4^- concentration at the membrane interface to drive diffusion and migration fluxes which oppose the advection flux. This buildup may also impact BH_4^- crossover, which has been observed under some conditions in DBFC experiments using Nafion membranes. [43].

Water crosses the membrane at a channel-averaged rate of 8.3×10^{-3} kg m^{-2} s^{-1} in the baseline case at 2.2 V, which is 14.6 times larger than the rate of water production at the anode. Large water crossover rates have been observed in experiments [44] and can be problematic for systems with large recirculation fractions. The permeation water flux (5.5×10^{-11} kg m^{-2} s^{-1}) is insignificant due to the small ($\sim$5 Pa) pressure difference across the membrane. The pressure difference across the membrane would have to be impractically high for the permeation flux to offset the electroosmotic drag flux.

Contour plots of species concentration in the channel (Fig. 4) are not a quantitative performance metric, but they can provide insight into cell operation. For example, the compact BH_4^- and BO_2^- concentration boundary layers near the anode explain why the fuel utilization is low; most fuel is carried through the channel before it can diffuse or migrate to the anode. Similarly, the Na$^+$ concentration boundary layer at the anode can be explained by diffusion, migration and advection interacting with the electroneutrality condition. The electric field drives cations away from the anode, but the Na$^+$ flux must be zero there because the wall is impermeable and Na$^+$ does not participate in the reaction. The Na$^+$ concentration near the anode is depressed to create a diffusion flux that opposes the migration flux and makes the net flux zero. Anion (BH_4^- and BO_2^-) concentrations must also decrease to maintain a neutral solution, and the lower anion concentrations change the rates of transport and local OCV.

3.2. Effects of reaction rate constant

Fast forward reaction rate constants were chosen for the baseline case to emphasize transport processes, but catalysts in DBFC experiments are often less active [15,45]. Slower anode rates were examined to understand how a less active anode catalyst would affect cell performance. Three polarization curves in Fig. 5 were generated by varying the anode forward reaction rate constant $k_{1,a}$ between 10^0 and 10^6 m^4 mol^{-1} s^{-1} with the cathode forward reaction rate constant $k_{2,c} = 10^6$ m^4 mol^{-1} s^{-1}. This range of rate constants corresponds to a shift in activation energy barrier E_{act} of approximately 35 kJ mol^{-1} (0.35 eV), which should encompass the range of uncertainty for a selected catalyst. The trend in Fig. 5 with increasing reaction rate constant (lower E_{act}) indicates performance benefits that may be obtained with the development of more active anode catalysts for the desired reactions. A faster anode reaction rate decreases the anode activation overpotential, but with diminishing returns for $k_{1,a} > 10^6$ m^4 mol^{-1} s^{-1}, beyond which point the anode activation overpotential is much smaller than other overpotentials in the cell.

A fourth polarization curve in Fig. 5 was generated using rate constants from the literature for BH_4^- oxidation on Pt ($k_{1,a} = 10^{-2}$ m s^{-1} [15]) and H$_2$O$_2$ reduction on Pt ($k_{2,c} = 8 \times 10^{-3}$ m s^{-1} [45]). This curve shows that using Pt at both electrodes will incur large activation losses, and peak power density will be lower (0.175 W cm^{-2}) compared to the transport dominated baseline case (1.06 W cm^{-2}). For comparison, power densities of 0.05–0.50 W cm^{-2} are typical of DBFC experiments, depending on cell design, operating conditions and catalyst selection [8].

Sensitivity to reaction rate was evaluated by changing the forward reaction rates at both electrodes from the baseline values. Comparing ASR plots in Fig. 2(c) ($k_{1,a} = k_{2,c} = 10^6$ m^4 mol^{-1} s^{-1}) to Fig. 6 ($k_{1,a} = k_{2,c} = 10^3$ m^4 mol^{-1} s^{-1}) shows that the anode activation ASR falls much faster than the cathode activation ASR when the forward rate constants are increased. For the conditions modeled here, the anode activation overpotential is therefore more sensitive to forward reaction rate constant.

3.3. Effects of cell geometry

For the cell topology illustrated in Fig. 1, two dimensions pertinent to cell performance are channel and membrane thickness. The electrolyte solutions (in the channels) and the membrane each have an electrical resistivity determined by the mobilities of charged species in the respective phase. The electrical resistivity incurs an ohmic loss (and associated ASR) which is reduced as the channel or membrane is made narrower. Furthermore, a narrower channel also results in a steeper voltage gradient in the y-direction which produces a stronger electric field and larger migration fluxes. The larger migration fluxes can augment electrode reactions and transport through the membrane.

Fig. 7 plots power density vs. cell potential for channels 0.50, 0.75 and 1.00 mm deep. The same mean fuel solution inlet velocity (0.1 m s^{-1}) was used in each case to eliminate changes in the rate of convection related to velocity. Shallower channels clearly provide higher power density with little sacrifice of voltage efficiency. This benefit is amplified further when considering volumetric power density because the shallower channels enable more cells to fit in a given volume. A further advantage of shallower channels is higher channel fuel utilization. With shallower channels, the concentration boundary layer occupies a larger fraction of the channel and therefore less fuel flows through the channel unreacted. Other performance metrics are listed in Table 6.

Most of the ohmic voltage loss between the two electrodes occurs in the membrane as shown in Fig. 8, with the losses being highest near the channel inlet where the current densities are highest. This is due to the relatively low diffusivity of Na$^+$ in Nafion (6.93×10^{-10} m^2 s^{-1} vs. 1.33×10^{-9} m^2 s^{-1} in water at infinite dilution). A thinner membrane mitigates these losses and improves the cell voltage and power density as illustrated in Fig. 9, where polarization and power density curves are plotted for three
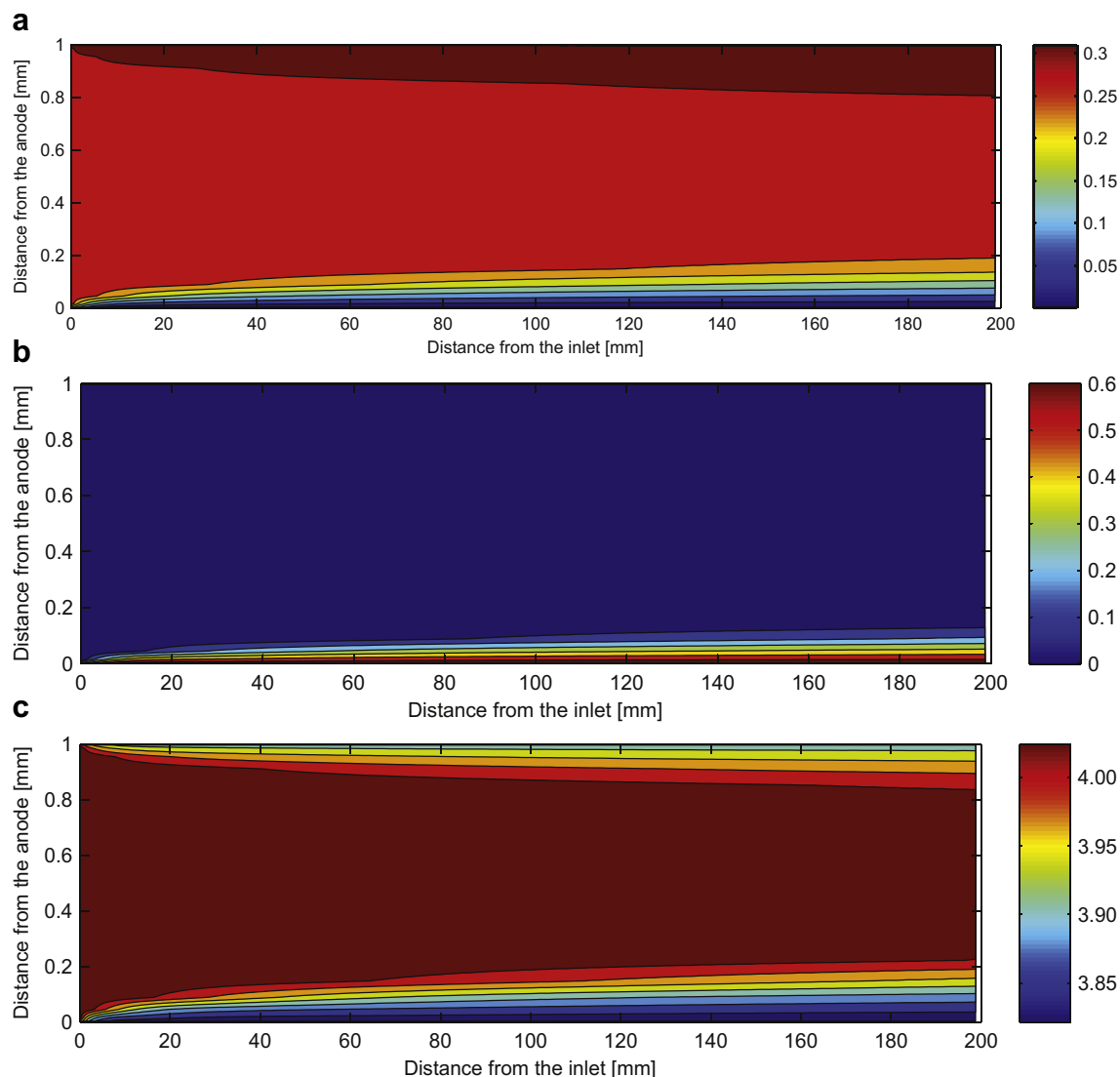
Fig. 4. Contour plots of (a) BH_4^-, (b) BO_2^- and (c) Na^+ concentration (kmol m^{-3}) in the fuel channel for the baseline case at 2.2 V (peak power density). Plots (a) and (b) show the development of concentration boundary layers at the anode as BH_4^- diffuses toward the anode and BO_2^- diffuses away from the anode. In plot (c) the boundary layer near the anode is a result of the zero-flux boundary condition for Na^+, and the boundary layer near the membrane is produced by Na^+ leaving the channel through the membrane.

membrane thicknesses. Reducing membrane thickness from 145 to 1.45 μm (equivalent to increasing membrane conductivity by 100 times) raises the cell voltage at 0.40 A cm^{-2} from 2.375 V in the baseline case to 2.570 V. The very thin 1.45 μm-thick membrane accounts for only 3.8–4.6% of the total ohmic losses in the cell (depending distance from the inlets). Of course, the risk of fuel crossover not considered in this model would become much more significant with such a thin membrane and would need to be included in a final analysis. Performance metrics as a function of membrane thickness without including the impact of fuel crossover are listed in Table 7.

3.4. Effects of fuel concentration and flow rate

Changes to fuel concentration and flow rate affect cell performance by changing concentrations near the electrodes, thereby changing the concentration overpotentials. Higher inlet BH_4^- concentration provides a larger gradient to drive BH_4^- from the bulk to the anode, which leads to higher fuel concentration near the anode. Higher flow rate improves convection transport of reactants to the

anode and products from the anode. Both scenarios increase power density by decreasing the concentration overpotential, increasing current density, or both.

A plot of power density vs. cell voltage (see Fig. 10) for a range of reasonable BH_4^- inlet concentrations between 0.1 and 0.5 M shows that peak power density is approximately proportional to the BH_4^- inlet concentration. The rate of peak power density increase with concentration slows at higher concentrations (see Fig. 10 inset) because other losses in the cell (ohmic and concentration overpotentials) play a larger role with increasing current density. Because the inlet BH_4^- concentration affects cell performance by altering the concentration overpotential, the strength of the effect depends on cell current density. At high current density the concentration overpotential is large, and increasing the BH_4^- inlet concentration can increase the power density substantially. The fuel utilization at high current density does not change with inlet BH_4^- concentration because both the rate of BH_4^- flow through the cell and the rate of consumption are proportional to concentration. At low current density the concentration overpotential is already small compared to other losses in the cell, so there is little
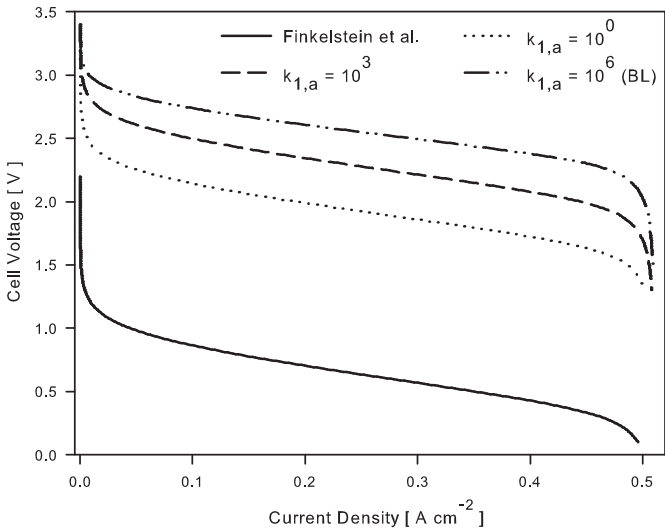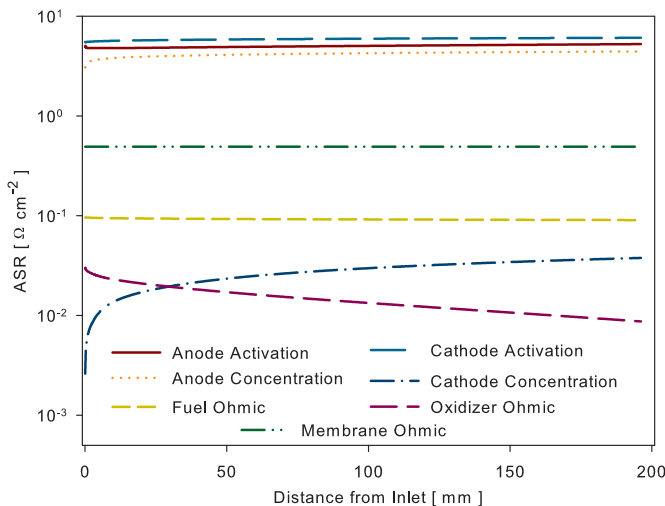
Fig. 5. Polarization curves with anode forward reaction rate constants of 10^0, 10^3 and 10^6 m^4 mol^{-1} s^{-1} and a cathode forward reaction rate constant of 10^6 m^4 mol^{-1} s^{-1}. The bottom curve assumes forward reaction rate constants from Finkelstein et al. on Pt; anode: 10^{-2} m s^{-1} and cathode: 8×10^{-3} m s^{-1}. All parameters, other than rate constants, are the same as in the baseline case, given in Table 4.

Fig. 7. Average power density vs. cell potential for channels that are 0.50, 0.75 and 1.00 mm deep. Aside from channel depth, all parameters are the same as in the baseline case, which is labeled "BL". The bold dashed curve is drawn through the maximum power density at each channel depth and describes the combinations of channel depth and cell voltage which yield peak power. In each case the mean velocity of fuel solution entering the fuel channel was 0.1 m s^{-1}.
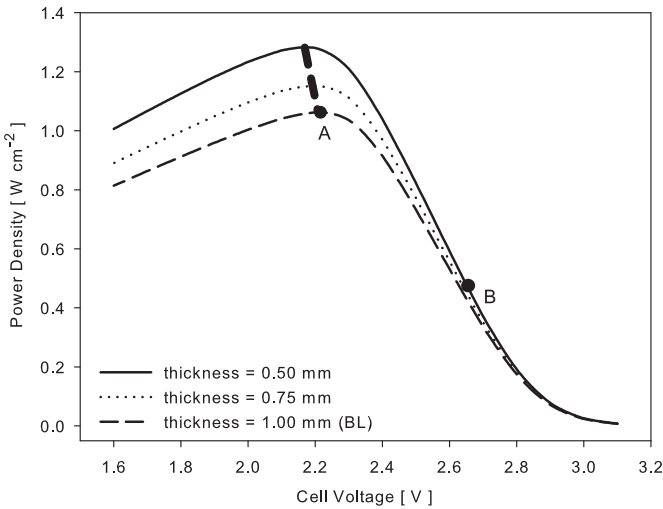
opportunity for higher BH_4^- inlet concentration to affect performance. Furthermore, at low current density the additional fuel goes unreacted, substantially decreasing fuel utilization.

The choice of inlet fuel concentration in a DBFC system depends on whether a recirculation loop is used. Recirculation is necessary in practical DBFCs to achieve acceptable system-level fuel utilization. Given practical lower bounds on fuel flow rate and channel depth, the single-pass fuel utilization will be low − in the case of this study, no greater than 10%. If a recirculation loop is used, it may be preferable to store the fuel at high concentration near the saturation limit and add it to the recirculation loop slowly to maintain low (~ 0.1 M) concentration in the cell. The low fuel concentration in the cell will yield lower peak power density (as shown in Fig. 10) but will mitigate losses to hydrolysis (Reaction (R4)).

Power density is plotted vs. cell voltage for three fuel flow rates in Fig. 11. The power density increases with increasing flow rate at

all current densities as the higher rates of transport change concentrations near the anode. The pressure drop in the channel increases in proportion to the flow rate, but the fuel utilization falls as indicated in Table 8. Increasing the fuel flow rate by a factor of four increases the pressure drop (pumping losses) by a factor of four, but only increases the peak power by 48%.

3.5. Implications for cell design

The results in Sections 3.1–3.4 can guide DBFC design by showing how performance varies with operating conditions and cell design parameters. For conditions in which cell performance is controlled by transport, the assumptions regarding reaction kinetics and OCV are reasonable, and the model can be used to compare specific design options. For example, Fig. 10 can be used to choose an inlet BH_4^- concentration by drawing a line through the peak power density of each curve. The dashed line in Fig. 10 demarcates the trade space maximizing power density as a function of BH_4^- inlet concentration and cell voltage. The region to the right of the dashed line describes designs or operating points which trade power density for higher voltage efficiency. Since the energy density of a system is proportional to fuel concentration, voltage efficiency and fuel utilization, moving to the right in Fig. 10 can substantially increase the system energy density. The maximum power density achievable given an energy density requirement (or vice versa) can be estimated from Fig. 10.

In general, shallower channels are preferable because they increase system-level power and energy density. Power density is improved when shallower channels decrease the stack volume, and

Fig. 6. Area specific resistance at points down the channel, for the case with forward reaction rates set to 10^3 and cell voltage of 2.2 V. Aside from the reaction rate constants, all parameters are the same as in the baseline case.

Table 6
Performance metrics with respect to channel depth. All other parameters are same as the baseline case.

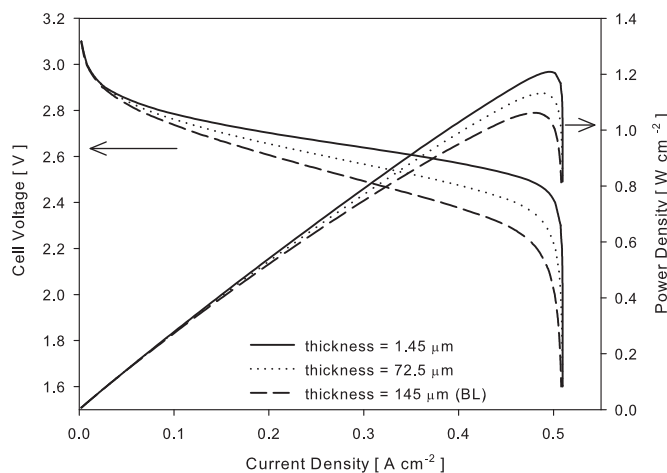| Parameter	Channel depth [mm]		
	0.50	0.75	1.00
Peak power density [W cm^{-2}]	1.28	1.15	1.06
Cell voltage@peak power density [V]	2.16	2.19	2.21
Fuel utilization@peak power density [%]	10.2	6.05	4.14
Power density@2.5 V [W cm^{-2}]	0.82	0.77	0.73
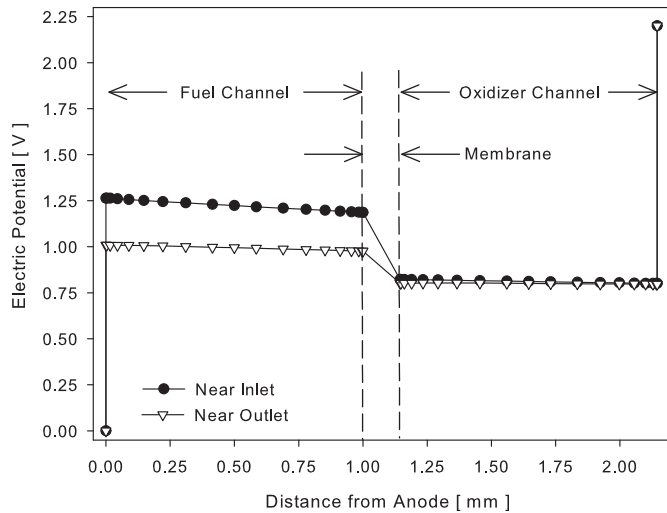
Fig. 8. Electric potential profiles across the cell from anode to cathode, near the inlet and near the outlet. The membrane clearly makes the largest contribution to the total ohmic loses, and the decrease in ohmic losses from inlet to outlet is related to the decrease in current density. Data in this figure are from the baseline at 2.2 V.
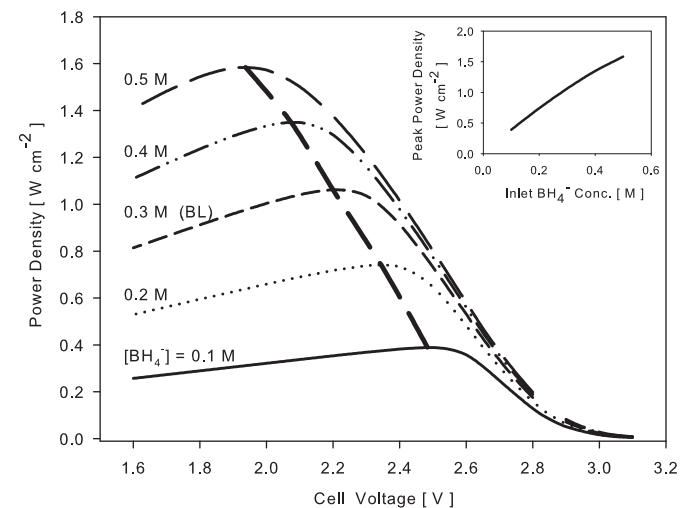
Table 7
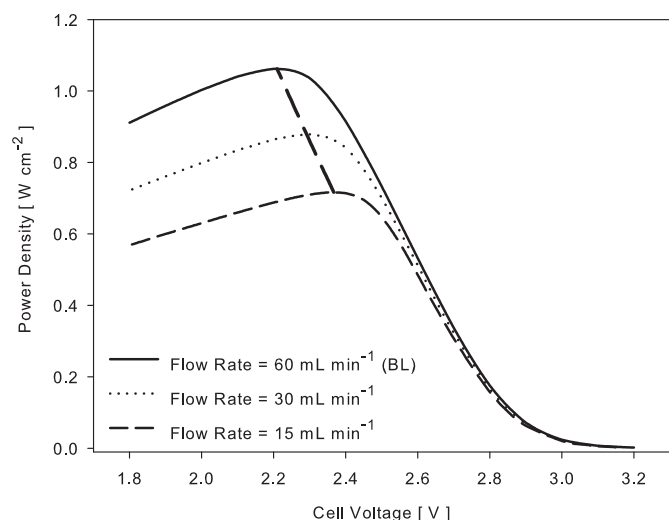Performance metrics with respect to membrane thickness. All other parameters are same as the baseline case.

Parameter	Membrane thickness [μm]				
	1.45	35.25	72.50	108.75	145.00
Peak power density [W cm^{-2}]	1.21	1.17	1.13	1.10	1.06
Cell voltage@peak power density [V]	2.43	2.37	2.32	2.26	2.21
Fuel utilization@peak power density [%]	4.26	4.24	4.19	4.17	4.14
Power density@2.5 V [W cm^{-2}]	1.18	1.07	0.94	0.82	0.73

energy density is improved when the smaller stack frees additional volume for reactant storage. When the additional volume is used to add active area to the stack, then it can produce the same power at lower current density and operate more efficiently (higher voltage per cell). These trends are seen in the DBFC model results. For example, a stack with channels 1.00 mm deep operating at 2.21 V per cell (point A in Fig. 7) would have the same volumetric power density as a stack with twice as many 0.50 mm deep channels operating at 2.64 V per cell (point B in Fig. 7), but the stack with shallower channels would have 36% less voltage loss. Channel fuel utilization is lower in the shallow channel case (3.2% vs. 4.2%) because of the lower current density, so a complete system trade would have to include the recirculation fraction and fuel storage density to find an optimum channel depth.

Another performance trade is the increase in peak power vs. parasitic power consumed by the fuel and oxidizer pumps. Table 8 shows that pressure drop through the fuel channel is directly

proportional to the fuel flow rate, as expected for laminar incompressible flow through a straight channel. The peak power is also proportional to the fuel flow rate, but increases at a rate of less than 8 mW cm^{-2} per mL min^{-1} increase in fuel flow rate. Thus, there may be a design point beyond which the additional power from faster flow is not worth the increase in pressure drop and loss of fuel utilization.

The low channel fuel utilization in all cases in this study bolsters experimental observations that any practical DBFC will require recirculation of the reactants to achieve high (>90%) overall fuel utilization. The near irreversibility of the borohydride oxidation reaction makes the reaction rate insensitive to BO_2^- concentration; reaction rates varied by less than 0.3% in simulations with BO_2^- inlet concentrations between 10^{-6} M and 0.3 M. The insensitivity to BO_2^- concentration makes extrapolating from once-through simulation results to a recirculating system straightforward because the only parameter related to both cell performance and the recirculation fraction is the BH_4^- concentration at the inlet. A simple recirculation model was constructed which interpolates among the results from the DBFC model with varying inlet concentration of BH_4^-. The recirculation model was used to investigate the relationships between anode recirculation volume fraction, fuel utilization and power density. The results for one case are shown in Fig. 12, in which the NaBH$_4$ fuel is stored at 0.5 M, the cell voltage is 2.5 V and fuel solution is added upstream of the channel at the same volumetric rate waste is rejected downstream of the channel. Fig. 12

Fig. 9. Polarization and power density curves for membrane thicknesses of 1.45, 72.5, and 145 μm. All other parameters are the same as in the baseline case, which is labeled "BL". The thickness of fully hydrated Nafion 115 in the Na$^+$ form is 145 μm [52]. Note that decreasing the membrane thickness is approximately equivalent to increasing the membrane conductivity by the same factor.

Fig. 10. Average power density vs. cell potential for fuel inlet concentrations ranging from 0.1 M to 0.5 M. All other parameters are the same as in the baseline case, which is labeled "BL". The bold dashed curve is drawn through the maximum power density at each concentration and describes the combinations of inlet concentration and cell voltage which yield peak power.

Fig. 11. Power density vs. cell voltage curves for fuel solution flow rates of 15, 30 and 60 mL min⁻¹. All other parameters are the same as in the baseline case, which is labeled "BL". The bold dashed curve is drawn through the maximum power density at each flow rate and describes the combinations of flow rate and cell voltage which yield peak power.

Table 8
Performance metrics with respect to fuel flow rate. All other parameters are same as the baseline case.

Parameter	Inlet fuel flow rate [mL min⁻¹]		
	15	30	60
Peak power density [W cm⁻²]	0.72	0.88	1.06
Cell voltage@peak power density [V]	2.37	2.29	2.21
Fuel utilization@peak power density [%]	10.5	6.60	4.14
Power density@2.5 V [W cm⁻²]	0.65	0.70	0.73
Channel pressure drop [Pa]	51.7	104	210

shows that the fuel utilization improves by a factor of more than 5 over a once-through approach when 99% of the fuel flow is recirculated, at the cost of a 50% decrease in power density due to the lower inlet BH_4^- concentration.

4. Conclusions

A 2-D DBFC model has been developed which captures the major losses (activation, ohmic and concentration) and down-the-channel effects in a DBFC with simple cell geometry. The results presented here assume simple electrode reaction models, but the model framework can accommodate competing reactions and mixed potentials when the mechanism and rate parameters for borohydride oxidation are better understood. The DBFC model was used to explore performance trends for conditions in which the ideal reactions are good approximations to the actual rates. The results show that transport due to advection, diffusion and migration all play an important role in the boundary layers developed at the electrode-channel and membrane–channel interfaces. The relative importance of these transport mechanisms evolves as the flow proceeds down-the-channel because concentration boundary layers develop and strongly affect cell behavior by shifting local concentrations and equilibrium. Models attempting to predict DBFC performance in cells with geometry similar to Fig. 1 must account for the change in conditions at points far from the inlet, preferably in an explicit manner as in this work.

Cells similar to Fig. 1 should have channels as shallow as practicable to increase fuel utilization and decrease ohmic losses in the
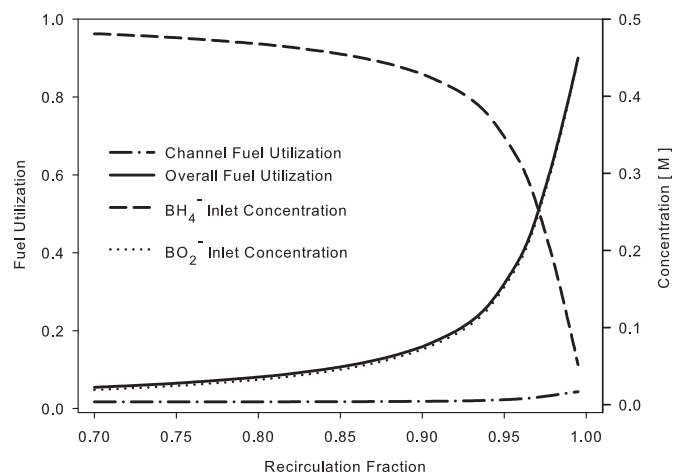
Fig. 12. Channel fuel utilization, overall fuel utilization, BH_4^- and BO_2^- concentrations at the inlet, all as functions of the fuel recirculation volume fraction. The concentration of BH_4^- in the fuel added to the recirculation loop was assumed to be 0.5 M. Aside from the inlet concentrations, all parameters are the same as in the baseline case.

fuel and oxidizer solutions. DBFC performance (peak power density, voltage efficiency and fuel utilization) rises more quickly than pumping losses, so any channel depth reduction yields a net gain in performance. Membranes are similar in that thinner membranes are preferable in the absence of fuel crossover. Higher fuel flow rates yield higher peak power density with slightly improved voltage efficiency, but with lower fuel utilization and increased pumping losses which vary with cell geometry. Water crossover from fuel channel to oxidizer channel must be addressed in a practical DBFC system using recirculation.

The sensitivity of DBFC performance to design and operating parameters encourages the use of a model when designing for a specific application. As illustrated here, there are many ways to adjust the power and similarly, energy density of a DBFC system by trading peak power density, voltage efficiency, fuel utilization, and recirculation fraction. A model can guide DBFC designers to a point closer to the final design before starting expensive prototype design-build-test iterations. Future work to calibrate the model against DBFC experiments and to incorporate a more comprehensive multi-step reaction mechanism into the model will provide increased confidence that the calibrated model can be used to design DBFC systems for various applications.

Appendix A. Nomenclature

a	anodic parameter (subscript)
β	electrochemical reaction symmetry factor
c	cathodic parameter (subscript)
ch	channel discretization (subscript)
C_k	concentration of species k
δ_k	apparent molar volume of species k in water
D_k	diffusivity of species k
E_R^0	standard half cell potential for reaction R
e_i	electrode interface discretization (subscript)

F	Faraday's constant
f	$F/R_{ig}T$
g_k	reaction rate order with respect to species k
h	channel depth
i	current density
$\vec{J}$	mass flux
$\vec{J}_k$	mole flux of species k
k_q	rate constant for reaction q
ℓ	roughness factor
μ	kinematic viscosity
m_i	membrane interface discretization (subscript)
n_d	electro-osmotic drag coefficient
n_e	number of electrons in the rate limiting reaction step
n_{elec}	number of electrons transferred per mole of fuel consumed
ϕ	electric potential
P	pressure
p_{H_2O}	membrane permeability to water
ρ	solution mass density
ρ_c	net charge density
R	residual (error) in model governing equation
R_{ig}	ideal gas constant
r_q	rate of reaction q
T	temperature
u_k	mobility of species k
v	velocity
v_k	stoichiometric coefficient of species k
V	volumetric flow rate
W_k	molar mass of species k
x	coordinate axis parallel to membrane
y	coordinate axis perpendicular to membrane
Y_k	mass fraction of species k
z_k	charge number of species k

References

[1] C.P. de Leon, F.C. Walsh, A. Rose, J.B. Lakeman, D.J. Browning, R.W. Reeve, J. Power Sources 164 (2007) 441–448.
[2] R.K. Raman, N.A. Choudhury, A.K. Shukla, Electrochem. Solid State Lett. 7 (2004) A488–A491.
[3] D.M.F. Santos, C.A.C. Sequeira, Alkaline Electrochem. Power Sources 25 (2010) 111–122.
[4] C.P. de Leon, F.C. Walsh, C.J. Patrissi, M.G. Medeiros, R.R. Bessette, R.W. Reeve, J.B. Lakeman, A. Rose, D. Browning, Electrochem. Commun. 10 (2008) 1610–1613.
[5] R.C. Urian, C.J. Patrissi, S.P. Tucker, C.M. Deschenes, F.W. Bielwaski, D.W. Atwater, in: Proceedings of the 43rd Power Sources Conference vol. 43, 2008, pp. 295–298.
[6] R.C. Urian, Material Res. Soc. Symp. Proc. 1213 (2010).
[7] M. Pourbaix, Atlas of Electrochemical Equilibria in Aqueous Solutions, second English ed., National Association of Corrosion Engineers, Houston, Texas, 1974.
[8] I. Merino-Jimenez, C.P. de Leon, A.A. Shah, F.C. Walsh, J. Power Sources 219 (2012) 339–357.
[9] J. Ma, N.A. Choudhury, Y. Sahai, Renew. Sust. Energy Rev. 14 (2010) 183–199.
[10] B.H. Liu, Z.P. Li, J. Power Sources 187 (2009) 291–297.
[11] G. Rostamikia, M.J. Janik, Energy Environ. Sci. 3 (2010) 1262–1274.
[12] G. Rostamikia, A.J. Mendoza, M.A. Hickner, M.J. Janik, J. Power Sources 196 (2011) 9228–9237.
[13] B.H. Liu, J.Q. Yang, Z.P. Li, Int. J. Hydrogen Energy 34 (2009) 9436–9443.
[14] G. Rostamikia, M.J. Janik, Electrochim. Acta 55 (2010) 1175–1183.
[15] D.A. Finkelstein, N. Da Mota, J.L. Cohen, H.D. Abruna, J. Phys. Chem. C 113 (2009) 19700–19712.
[16] E. Gyenge, Electrochim. Acta 49 (2004) 965–978.
[17] U.B. Demirci, J. Power Sources 172 (2007) 676–687.
[18] D.M.F. Santos, P.G. Saturnino, D. Maccio, A. Saccone, C.A.C. Sequeira, Catal. Today 170 (2011) 134–140.
[19] B.H. Liu, Z.P. Li, S. Suda, Electrochim. Acta 49 (2004) 3097–3105.
[20] D.M.F. Santos, C.A.C. Sequeira, J. Electrochem. Soc. 156 (2009) F67–F74.
[21] B.M. Concha, M. Chatenet, Electrochim. Acta 54 (2009) 6119–6129.
[22] K.S. Freitas, B.M. Concha, E.A. Ticianelli, M. Chatenet, Catal. Today 170 (2011) 110–119.
[23] S.C. Amendola, P. Onnerud, M.T. Kelly, P.J. Petillo, S.L. Sharp-Goldman, M. Binder, J. Power Sources 84 (1999) 130–133.
[24] W.H. Stockmayer, C.C. Stephenson, J. Chem. Phys. 21 (1953) 1311–1312.
[25] W. Stockmayer, R.J. Zeto, R.R. Miller, J. Phys Chem — US 65 (1961) 1076.
[26] D.X. Cao, L.M. Sun, G.L. Wang, Y.Z. Lv, M.L. Zhang, J. Electroanal. Chem. 621 (2008) 31–37.
[27] V.R. Choudhary, C. Samanta, T.V. Choudhary, J. Mol. Catal. A Chem. 260 (2006) 115–120.
[28] L.F. Gu, N. Luo, G.H. Miley, J. Power Sources 173 (2007) 77–85.
[29] S. Townea, M. Carellab, W.E. Mustainb, V. Viswanathana, P. Riekea, U. Pasaogullaric, P. Singhb, ECS Trans. 25 (2009) 1951–1957.
[30] R.C. Urian, Mater. Res. Soc. Symp. Proc. 1168 (2009).
[31] A. Verma, S. Basu, J. Power Sources 168 (2007) 200–210.
[32] A.E. Sanli, M.L. Aksu, B.Z. Uysal, Int. J. Hydrogen Energy 36 (2011) 8542–8549.
[33] A.A. Shah, H. Al-Fetlawi, F.C. Walsh, Electrochim. Acta 55 (2010) 1125–1139.
[34] A.A. Shah, R. Singh, C.P. de Leon, R.G. Wills, F.C. Walsh, J. Power Sources 221 (2013) 157–171.
[35] I.B. Sprague, P. Dutta, Numer. Heat Transfer Appl. 59 (2011) 1–27.
[36] I. Sprague, P. Dutta, Electrochim. Acta 56 (2011) 4518–4525.
[37] A.C. Hindmarsh, P.N. Brown, K.E. Grant, S.L. Lee, R. Serban, D.E. Shumaker, C.S. Woodward, ACM Trans. Math. Software 31 (2005) 363–396.
[38] E.S. Oran, J.P. Boris, Numerical Simulation of Reactive Flow, second ed., Cambridge University Press, Cambridge, U.K.; New York, 2001.
[39] J.S. Newman, K.E. Thomas-Alyea, Electrochemical Systems, third ed., J. Wiley, Hoboken, N.J., 2004.
[40] H. Cheng, K. Scott, K. Lovell, J.A. Horsfall, S.C. Waring, J. Membr. Sci. 288 (2007) 168–174.
[41] A.J. Bard, L.R. Faulkner, Electrochemical Methods: Fundamentals and Applications, second ed., Wiley, New York, 2001.
[42] H. Cheng, K. Scott, Electrochim. Acta 51 (2006) 3429–3433.
[43] H. Cheng, K. Scott, J. Power Sources 160 (2006) 407–412.
[44] S. Lux, L.F. Gu, G. Kopec, R. Bernas, G. Miley, J. Fuel Cell Sci. Technol. 7 (2010).
[45] D.A. Finkelstein, J.D. Kirtland, N. Da Mota, A.D. Stroock, H.D. Abruna, J. Phys. Chem. C 115 (2011) 6073–6084.
[46] D.M.F. Santos, C.A.C. Sequeira, J. Electrochem. Soc. 157 (2010) F16–F21.
[47] C.R. Cloutier, A. Alfantazi, E. Gyenge, THERMEC 2006 Suppl. 15–17 (2007) 267–274.
[48] G. Ottonello, Principles of Geochemistry, Columbia University Press, New York, 1997.
[49] W.C. Schumb, Hydrogen Peroxide, Reinhold Pub. Corp, New York, 1955.
[50] J.M. Nielsen, A.W. Adamson, J.W. Cobble, J. Am. Chem. Soc. 74 (1952) 446–451.
[51] A. Poisson, J. Chanu, Mar. Chem. 8 (1980) 289–298.
[52] T. Okada, S. Moller-Holst, O. Gorseth, S. Kjelstrup, J. Electroanal. Chem. 442 (1998) 137–145.
[53] T. Okada, H. Satou, M. Okuno, M. Yuasa, J. Phys. Chem. B 106 (2002) 1267–1273.
[54] C.E. Evans, R.D. Noble, S. Nazeri-Thompson, B. Nazeri, C.A. Koval, J. Membr. Sci. 279 (2006) 521–528.